

# CHAPTER 22

## Portable force feedback device based on miniature rolled dielectric elastomer actuators

Rui Zhang<sup>a</sup>, Patrick Lochmatter<sup>a</sup>, Gabor Kovacs<sup>a</sup>, Andreas Kunz<sup>b</sup>, François Conti<sup>c</sup>

<sup>a</sup>*Laboratory for Mechanical Systems Engineering, Swiss Federal Laboratories for Materials Testing and Research (Empa), Duebendorf, Switzerland*

<sup>b</sup>*Institute of Machine Tools and Manufacturing, Swiss Federal Institute of Technology (ETH), Zurich, Switzerland*

<sup>c</sup>*Artificial Intelligence Laboratory, Stanford University, California, USA*

### 22.1 Introduction

Virtual reality (VR) can be traced back to about fifty years ago when Morton Heilig, a cinematographer, began designing the first multi-sensory virtual experiences. In order for spectators to be fully immersed in a film scene, he developed the “Sensorama Simulator” which added to the projected film, sounds, vibrations, wind and even odors [1]. Nowadays, after a remarkable and complex history [2], VR has led to a wide range of multi-sensory applications for entertainment and professional purposes [3-6].

While VR has strongly benefited from the important progresses in computer technology, there still remain limitations with the current techniques for including the stimulation of the sense of touch. Unlike graphical displays, which can render large photographic images at very high resolution, tactile displays can only generate limited forces within small punctual areas. With the appearance of new medical robotic tools to perform minimal invasive procedures in a more precise way in recent years, however, there has been an increasing demand for more robust and efficient force feedback devices (FFD) which allow users to instinctively grasp, feel and manipulate virtual or real objects [7].

In respect of their location, current FFDs can generally be classified into the categories of *ground-based* and *body-based* devices. Ground-based devices are fixed to the environment such as a desk, a wall, the ceiling, or the floor, while body-based devices are attached to the human body, for instance to the shoulders, arms, legs, or hands.

Stylus apparatus such as the PHANTOM [8] and the Delta [9] provide continuous point contact forces in six degrees of freedom (DOF), and therefore, are leading ground-based solutions in gripper or end-effector designs. However, implicit friction and backlash, limited physical workspace and the absence of portability remain significant drawbacks.

Body-based devices conventionally consist of a hand-exoskeleton structure [3, 11-14]. These devices are portable and provide thus access to large working space in a virtual environment. However, this portability is achieved at the cost of limited ergonomics since the user needs to carry the device as a

whole or part of it. In addition, the limited design space for the FFD, placed either on the palmar or on the dorsal side of the hand, makes the selection of an appropriate actuator technology quite challenging, and requires complex design of the force transmission structure.

In this chapter, a FFD based on electroactive polymers (EAPs) is presented. As promising driving elements for the FFD, rolled actuators from soft dielectric EAP are proposed. Theoretical considerations address the electromechanical behavior of rolled dielectric elastomer (DE) actuators under activation. Experimental characterization results show the potential of the miniature rolled DE actuators for their application to FFDs. Given the high driving voltages in the range of several kilovolts needed for DE actuators, electrical safety issues are discussed. Finally, two force feedback demonstration devices are presented.

## 22.2 Force feedback system

### 22.2.1 Components and principle of operation

Fig. 22.1 illustrates the overall scheme of a force feedback system. The graphical interface displays a computer-generated virtual environment [22] via a computer screen or a head-mounted display to the user. Within this simulated environment, the hand of the user is represented through a cursor or a graphical avatar. During the force feedback simulation, the system runs through the following steps: The sensing system captures the flexion of the joints of the user's fingers. This information is sent to the control computer for updating the configuration of the avatar. The control computer checks for possible collisions between the user's fingers represented by the avatar and the virtual object. In case of a collision, reaction forces are calculated and corresponding commands are sent to the controllers of the actuators. The specifically activated actuators exert thus forces to the contact areas of the user's hand. At the same time, the graphical representation of the VR is updated and presented to the user via the graphical interface.

In general, a FFD has to cover the following requirements to achieve a realistic force feedback:

- **Range of forces and directionality:** The device should be able to generate forces at given contact points as soon as an interaction between the hand and a virtual object occurs.
- **Backdriveability [10]:** The device should exhibit low passive intrinsic mechanical impedance so that the free motion of the fingers is not disturbed. Extending this definition, a device is also considered to be backdriveable if it can actively follow the free motion of the fingers.
- **Sensing bandwidth [7]:** The sensing bandwidth refers to the frequency with which tactile (for texture), and kinesthetic (for force) stimuli are sensed by the user. For a force feedback system, the interest is on the human kinesthetic bandwidth of 20-30 Hz.
- **Transparency [10]:** The transparency determines the ability of a device to reproduce the exact contact force computed by the virtual reality system when the user's fingers collide with a virtual object. Ideally, a user should not notice the weight, inertia, and internal friction of the device.

### 22.2.2 Conceptual approach

As schematically illustrated in Fig. 22.2, left, the contact with an object during precision grasping concentrates on the fingertips of the thumb, the index, the middle and the ring finger [15]. The fingers' flexion driven by the muscles and tendons in the hand and the forearm is blocked by the contact reaction forces,  $F_{object}$ , of the grasped object. Neglecting the weight of the object, these reaction forces are opposed and of equal strength to satisfy the static force equilibrium.

In order to simulate precision grasping in VR, a FFD must provide equivalent contact reaction forces,  $F_{device}$ , to the contact areas of the fingers as would arise from a real object ( $F_{object} = F_{device}$ ).

Conventional portable FFDs on the dorsal side of the hand (Fig. 22.2, center) need mechanically complex force transmission structures such as exoskeletons and cable-pulley structures [3,11,13,14], which makes them bulky and heavy. Due to the resulting internal friction and inertia such devices exhibit poor performance in mechanical transparency [10] and dynamics. Moreover, the attachment of the structure to the hand introduces undesired forces, which may bother the force feedback sensation.

One way to avoid force transmission structures is to directly attach the actuators to the contact areas of the user. Regarding grasping devices, the actuators may thus be located either on the palmar or on the dorsal side of the hand [7]. Following both approaches we evaluated various concepts for portable FFDs [16]. Due to minimum kinematics we finally selected the “hand-held” approach, where the actuators are directly connected between the thumb and the opposing fingers (Fig. 22.2, right).

### 22.2.3 Actuator evaluation

A “hand-held” FFD was implemented earlier by Bouzit [12] based on pneumatic actuators (Rutgers Master II). The concept was proved to be simple, compact, portable and capable to provide a very realistic grasping feedback of soft and rigid objects to the user. However, for their application to FFDs pneumatic actuators have some distinct disadvantages such as their large weight, static friction, operation noise and compressibility of the air in the cylinder. Moreover, they require an elaborate supply system (compressor, pressure regulator, control valves, air-supply lines).

For force feedback applications, a set of lightweight actuators providing a wide range of forces and passive or actively tracked free motions are needed. Furthermore, the actuators need to be safe, reliable, energy-efficient, and be supplied by a compact power source.

## 22.3 Miniature rolled dielectric elastomer (DE) actuators

According to preliminary investigations [17], rolled actuators based on soft dielectric EAPs are likely to meet the challenging requirements for their application to a “hand-held” FFD.

### 22.3.1 Design and manufacturing process

Rolled DE actuators consist of a stack of two biaxially pre-stretched DE films, which is wrapped around a fully compressed coil spring (Fig. 22.3). By introducing a telescopic guidance in the core of the actuator, even axial compressive loads can be taken. Miniature rolled DE actuators were fabricated based on a machine-aided manufacturing process [17].

### 22.3.2 Principle of operation

In the free-standing state, the coil spring is in force equilibrium with the pre-stretched DE film. In the axial direction, the elastomeric film is pre-stretched by the compressed coil spring, while in the radial direction the circumferentially pre-stretched film is supported by the coil spring core. Under activation the actuator expands in its axial direction ( $z$  direction). The actuator reaches its maximum active elongation under free axial boundary condition, while the maximum active force is obtained when the actuator is blocked in the axial direction (see Chapter 30).

### 22.3.3 Theoretical consideration

The theoretical consideration focuses on two particular issues of the rolled actuator configuration. In addition, an estimation of the axial force generation of rolled DE actuators as a function of voltage is given.

#### Non-uniform pressure distribution across the wrapped DE film

Wrapping of the biaxially pre-stretched film around the coil spring core causes the outer film layers to compress the inner ones. The resulting radial pressure on the inner film layers grows with increasing number of film wrappings as well as with stronger circumferential pre-stretching of the films. As a result, a strong gradient in axial stresses arises across the pre-strained film layers. While the outer film layers are still in the tensile domain the inner ones tend to expand in axial direction (Chapter 30). In order to thus properly fix all film layers, both ends of the rolled actuators were sealed with polymer (Fig. 22.3).

#### Non-uniform thickness distribution of the DE film under elongation

For simplification, we assume that in the free-standing, deactivated state ( $V = 0$ )  $N$  layers of pre-stretched DE film are concentrically stacked around the rigid spring core with radius  $R$  (Fig. 22.4, left). The inner radius of the  $n^{\text{th}}$  film layer is  $R_{n-1}^{(V=0)}$  and the corresponding outer radius is  $R_n^{(V=0)}$ . Hence, the thickness of the  $n^{\text{th}}$  film layer is  $d_n^{(V=0)} = d^{(i)} = R_n^{(V=0)} - R_{n-1}^{(V=0)}$ .

By applying the film’s incompressibility condition, the thickness,  $d_n^{(V=0)}$ , of the biaxially pre-stretched film (planar pre-stretch ratios  $\lambda_x^{(i)} \times \lambda_y^{(i)}$  in the pre-stretch state (i)) can be calculated based on the original film thickness,  $d^{(o)}$ , of the widely-used acrylic film VHB 4910 (by 3M) by

{Eq. (1)}.

Under free-strain activation ( $V > 0$ ), the electrostatic pressure squeezes the dielectric film in its thickness direction and thus the actuator elongates in its axial direction. When the actuator performs an axial strain of  $S_z$ , all film layers are axially elongated to the same degree (Fig. 22.4, center). Based on the volume conservation of each film layer  $n$ ,

{Eq. (2)}

the normalized thickness of the film layers in the actively elongated state ( $V > 0$ ) is obtained by

{Eq. (3)}

where the radius of the core is assumed to remain constant during elongation ( $R_o^{(V>0)} = R_o^{(V=0)} = R$ ). The recursive relationship Eq. (3) is evaluated for the miniature rolled DE actuators, whereby  $R = 7$  mm,  $d^{(0)} = 1$  mm and  $\lambda_x^{(i)} \times \lambda_y^{(i)} = 3 \times 6.5$ . The resulting normalized thickness distribution is exemplarily plotted in Fig. 22.4, right, for the film layers  $n = 1, 2, \dots, 60$  and selected axial strain levels,  $S_z$ , from 0 to 75%.

As can be seen, under axial elongation of rolled DE actuators the thickness of the inner film layers decreases significantly greater than that of the outer ones. This effect becomes more distinct for larger elongation in the axial direction. Under electrical activation of the actuator, this effect leads to an accumulation of electrical charges in the domain of the thinner film layers where thus the electrical field increases. Therefore, an electrical breakdown is estimated to occur primarily within the inner film layers of actively elongated, rolled DE actuators.

#### Axial force under blocked strain activation

The compressive force,  $F_{com}$ , needed to block the active elongation of a rolled DE actuator starting from the deactivated state ( $V = 0$ ) is derived as a function of the activation voltage,  $V$ . The stresses of the biaxially pre-stretched film (state (i)) are given by the Cauchy stresses,  $T_j^{(i)}$ , in the directions  $j = x, y, z$  (Fig. 22.5, left) by

{Eq. (4)}

when introducing the proper boundary conditions (in  $x$ :  $T_x = T_x^{(i)}$ ,  $\lambda_x = \lambda_x^{(i)}$ ; in  $y$ :  $T_y = T_y^{(i)}$ ,  $\lambda_y = \lambda_y^{(i)}$ ; in  $z$ :  $T_z = 0$ ,  $\lambda_z = \lambda_z^{(i)}$ ). Therein,  $w$  is the strain energy potential of the film,  $p_h^{(i)}$  is the hydrostatic pressure in the film, and  $\lambda_j^{(i)}$  is the film's pre-stretch ratio in the directions  $j = x, y, z$ .

The pre-stretched DE film is then wrapped around the coil spring core. We define that the  $x$  direction of the DE film points along the axis of the coil spring. Thus, the film's coordinates change from the planar to the cylindrical configuration according to  $x \rightarrow z$ ,  $y \rightarrow \varphi$ ,  $z \rightarrow r$  (Fig. 22.5).

We assume that the stretch state (i) of the biaxially pre-stretched film equals the stretch state of the wrapped film of the free-stranding, deactivated ( $V = 0$ ) rolled DE actuator. Furthermore, we take into account that the thickness of the pre-stretched film,  $d^{(i)}$ , is by far smaller than the radius,  $R$ , of the coil spring core ( $(d^{(i)}/R) \ll 1$ ). Thus, the equations for the Cauchy stresses in Cartesian coordinates according to Eq. (4) can be applied to all film layers  $n = 1, 2, \dots, N$  of the rolled DE actuator as well

{Eq. (5)}

by adapting the boundary conditions (in  $r$ :  $T_r = -p_{r,n}^{(V=0)}$ ,  $\lambda_r = \lambda_z^{(i)}$ ; in  $\varphi$ :  $T_\varphi = T_{\varphi,n}^{(V=0)}$ ,  $\lambda_\varphi = \lambda_y^{(i)}$ ; in  $z$ :  $T_z = T_{z,n}^{(V=0)}$ ,  $\lambda_z = \lambda_x^{(i)}$ ).

Under blocked strain activation ( $S_z = 0$ ), the geometry of the incompressible DE film is maintained since the actuator core is rigid and the actuator's length is maintained. The Cauchy stresses in the activated state ( $V > 0$ ) are obtained when the effective electrostatic pressure [18]

{Eq. (6)}

is superimposed in the radial direction ( $T_r = -p_{r,n}^{(V>0)} = -(p_{r,n}^{(V=0)} + p)$ )

{Eq. (7)}.

By combining Eqs. (4) to (7), the resulting compression force,  $F_{com}$ , can be derived

{Eq. (8)}.

Therein,  $F_{spring}^{(V=0)}$  is the spring force and  $A_{film,z}^{(V=0)}$  is the overall axial cross-sectional area of the DE film layers in the free-standing, deactivated state ( $V = 0$ ). As shown, under activation the effective electrostatic pressure,  $p$ , is transmitted from the radial direction via the hydrostatic pressure into the axial direction of the rolled actuator. Thus, a quadratic increase in compressive force,  $F_{com}$ , as a function of the activation voltage,  $V$ , is expected.

Taking into account the non-uniform thickness distribution of the wrapped film layers given by Eq. (3), the axial force,  $F_z^{(V>0)}$ , of an isometrically ( $S_z = const. \geq 0$ ) activated rolled DE actuator is predicted to decrease from the deactivated tensile force,  $F_z^{(V=0)}$ , according to

$$\{\text{Eq. (9)}\}.$$

#### 22.3.4 Experimental characterization of the rolled DE actuators

The actuators were mounted between a base frame and a pneumatic cylinder (Bramati by Empa Dubendorf), which actively controlled the displacement of the actuators. To measure the forces along the principal axis of the actuator, a load cell was implemented (U2B by HBM). The measurement signals were acquired via an adapter chassis (BNC 2090 by National Instruments) and a data acquisition card (PCI-6070e by National Instruments) and were processed by a LabVIEW program. Optoelectronic couplers (OK RB6200 by Relmatic) were used to isolate the high voltage from the low voltage circuit.

The actuators were characterized by isometric tests at different displacement levels from 0 to 8 mm for driving voltage levels from 0 to 3.5 kV.

From the tests, the force-displacement behavior (Fig. 22.6, left) and the force-voltage behavior (Fig. 22.6, right) were obtained. The force-displacement curves of the deactivated ( $V = 0$ ) as well as activated ( $V > 0$ ) actuator are quasi-linear. As expected, the force-displacement curves gradually shift to lower force levels for increasing activation voltages.

An average compressive force of 5.5 N was found when blocking the actuator's elongation in its free-standing state (blocking force). With free boundary condition in the axial direction an average displacement of 2.7 mm was reached (free displacement).

As shown in Fig. 22.6, left, a wide range of material characteristics (from soft to hard) of both sticky and non-sticky objects can be simulated by the miniature rolled DE actuators in force feedback applications.

From the test results, it was observed that the blocking force decreases quadratically as the applied voltage is increased (Fig. 22.6, right). This behavior is in qualitative agreement with the theoretical predictions according to Eqs. (8) and (9). However, for a quantitative agreement the theoretically estimated force development had to be reduced by a factor of 0.45 (dashed lines in Fig. 22.6, right,  $\varepsilon_r = 3.12$  [19]). The undershooting of the experimental performance may have originated from inhomogeneities of the used materials and imperfections introduced during the manufacturing of the actuators. The wide variance in measurement results from the tested actuators (the blocking force ranged from 1.47 to 7.2 N and the free displacement from 1 to 5 mm) points out the issue of unsatisfying reproducibility.

#### 22.4 Electrical safety issues

The investigation of the electrical failure behavior of the actuator-user system was based on an electrical model including the human user [23], the DE actuator, a power supply and connecting electric cables (Fig. 22.7). Possible failures of the system and thus endangerments to the user can occur mainly in two ways: The actuator is discharged through the human body (i) with or (ii) without being connected to the power supply (Fig. 22.7).

In the failure case (i), the human operator is subjected to the supply circuit of the actuator. According to [21], the current provided by the power supply has to be limited to 25 mA and is to be interrupted in failure case not later than 2 s. Beyond this limitation, disturbances of formation and conduction of

impulses in the heart may occur. Practically, this limitation was accomplished by integrating a residual current circuit breaker between the actuator and the power supply.

In the failure case (ii), a maximum effective current of 22 mA over an impulse duration of 7 ms corresponding to a discharge of 0.125 mC results for a driving voltage of 5 kV, resistances of  $R_a = 90 \text{ k}\Omega$  and  $R_s = 2.5 \text{ M}\Omega$ , a capacity of  $C_a = 25 \text{ nF}$ , an impedance of  $Z_i = 0.5 \text{ k}\Omega$  (current path hands to feet) and a copper cable length of 0.1 m (portable source). According to IEC 60479-2 [20], this discharge through the human body may cause pain at the contact area, but does not have harmful physiological effects. Regarding the actuator design further protective measures were taken by insulating the rolled DE actuator and by connecting the outermost electrode to ground potential.

### 22.5 Demonstration devices

Two force feedback demonstration devices based on the miniature rolled DE actuators were built. The first device consisted of a rolled actuator, which was mounted inside a transparent Perspex cylinder (Fig. 22.8, left). Holding both ends of the device, the user could feel the actively generated force and/or displacement of the actuator.

Secondly, a FFD according to the proposed “hand-held” concept was implemented, where three rolled DE actuators were attached via spherical joints between the thumb and the index, the middle, and the ring finger (Fig. 22.8, right).

### 22.6 Conclusions

In this chapter, we presented a transmission-free, portable force feedback device (FFD) driven by the miniature rolled dielectric elastomer (DE) actuators. The actuators exhibited a maximum blocking force (blocked boundary condition) of 7.2 N and a maximum elongation (free boundary condition) of 31% according to the active zone and 11% according to the overall length, respectively.

The implemented FFD operates noiseless and has a much lower mass (38 g) than existing devices such as the Rutgers Master II (185g) and the CyberGrasp (340 g).

From the studies on the failure mechanisms of electrical safety, we found that discharging of the miniature rolled DE actuators alone does not have harmful physiological effects on a human user. To protect the user from the energy delivered by the power supply, the failure current in the circuit was limited to 25 mA by a circuit breaker.

In the next steps, the proposed FFD has to be implemented in a control environment and extensive psychophysical tests have to be conducted (preliminary results in [17]). At the same time the electromechanical reliability of the rolled DE actuators needs to be significantly improved. To overcome the viscous restrictions (frequency limitation, energy losses) of the DE actuators from widely-used VHB 4910 (by 3M), appropriate dielectric films with purely elastic mechanical properties (e.g. silicone-based films) have to be developed [24]. A fully automated manufacturing process for the miniature rolled DE actuators is required to avoid poor reproducibility originating from manual production.

### 22.7 Acknowledgements

This study has been funded by the Swiss National Science Foundation (SNSF) and was greatly supported by the Swiss Federal Laboratories for Materials Testing and Research (Empa).

### References

- [1] Youngblut C. (1996) Review of Virtual Environment Interface Technology, *Tech. Rep. IDA Paper P-3186, Institute for Defense Analyses (IDA)*.
- [2] Hamit F. (1993) *Virtual reality and the exploration of cyberspace*, Sams Publishing.
- [3] [www.immersion.com](http://www.immersion.com).
- [4] Gausemeier J. (2004) A Virtual Reality-based Design Environment for Self-Optimizing Mechatronic Systems, In *Mechatronics & Robotics*, Eds. Drews, P. Eysoldt, Aachen, p. 1333-1339.
- [5] Spagno C. (2003) Construction of a Three-sided Immersive Telecollaboration System, *Proc. of IEEE VR*, LA, California, March 2003, p. 22-26.

- [6] Atkins J. E. (2003) Experience-dependent Visual Cue Recalibration based on Discrepancies between Visual and Haptic Percepts, *Vision Research*, **43**, p. 2603-2613.
- [7] Burdea G. C. (1996) *Force and touch feedback for virtual reality*, John Wiley & Sons, Inc.
- [8] www.sensable.com.
- [9] www.forcedimension.com.
- [10] Barbagli F. (2003) Enabling Multi-finger, Multi-hand Virtualized Grasping, *Proc. of IEEE International Conference of Robotics and Automation*, Taipei, 2003, p. 1259-1263.
- [11] Stergiopoulos P. (2003) Design of a 2-Finger Hand Exoskeleton for VR Grasping Simulation, *Proceedings of Eurohaptics 2003*, Dublin, Ireland, July, p.80-93
- [12] Bouzit M. (2002) The Rutgers Master II-New Design Force Feedback Glove, *IEEE/ASME Transactions on Mechatronics* **7**(2), p. 256-263.
- [13] Bouzit M. (1996) *Design, Implementation and Testing of a Data Glove with Force Feedback for Virtual and Real Objects Telemanipulation*. PhD Thesis, University of Pierre et Marie Curie.
- [14] Choi B. (2000) SKK Hand Master-Hand Exoskeleton Driven by Ultrasonic Motors, *Proc. of the 2000 IEEE/RS International Conference on Intelligent Robots and Systems*, Taipei, September, p. 1131-1136.
- [15] Cutkovsky M. (1990) Human Grasp choice and Robotic Grasp Analysis, In *Dextrous robot hands*, Eds. Venkataraman, S. T. and Iberall, T., Springer, New York , p. 5–31.
- [16] Zhang R. (2006) Dielectric Elastomer Spring Roll Actuators for a Portable Force Feedback Device, *Proc. of 14th Symposium on Haptic Interfaces for Virtual Environment and Teleoperator systems*, Arlington, Washington D.C. U.S.A, March, p.53
- [17] Zhang R. (2007) *Development of Dielectric Elastomer Actuators and their Implementation in a Novel Force Feedback Interface*, PhD thesis, ETH Zurich (in preparation).
- [18] Pelrine, R. (1998) Electrostriction of polymer dielectrics with compliant electrodes as a means of actuation, *Sensors and Actuators A: Physical* **64**(1), p. 77–85.
- [19] Wissler M. (2006) Electromechanical coupling in dielectric Elastomer actuators. *Sensors and Actuators A: Physical*, in press.
- [20] IEC (1987) *Effects of current passing through the human body, Part 2: Special effects*, IEC 60479-2, Second edition, International Electrotechnical Commission (IEC).
- [21] IEC (1994) *Effects of current on human beings and livestock. Part 1: General aspects*, IEC 60479-1, Third edition, *International Electrotechnical Commission (IEC)*.
- [22] Conti F. (2005) CHAI 3D - An Open-Source Library for the Rapid Development of Haptic Scenes, *Proc. of IEEE World Haptics*, Pisa, Italy, March.
- [23] Biegelmeier G.(2003) *Schutz in elektrischen Anlagen. Band one: Gefahren durch den elektrischen Strom*, VDE Verlag GmbH, Berlin.
- [24] Zhang X. (2004) Effects of crosslinking, prestrain, and dielectric filler on the electromechanical response of a new silicone and comparison with acrylic elastomer. *Proc. of Smart Structures and Materials 2004: Electroactive Polymer Actuators and Devices (EAPAD)*, San Diego, CA, V5385, p.78–86.

## Equations

$$d_n^{(V=0)} = d^{(i)} = \frac{d^{(o)}}{\lambda_x^{(i)} \lambda_y^{(i)}} \quad (1)$$

$$\pi \left( \left( R_n^{(V=0)} \right)^2 - \left( R_{n-1}^{(V=0)} \right)^2 \right) \cdot L = \pi \left( \left( R_n^{(V>0)} \right)^2 - \left( R_{n-1}^{(V>0)} \right)^2 \right) \cdot L (1 + S_z) \quad n = 1, 2, \dots, N \quad (2)$$

$$\frac{d_n^{(V>0)}}{d_n^{(V=0)}} = \frac{d_n^{(V>0)}}{d^{(i)}} = \frac{R_n^{(V>0)} - R_{n-1}^{(V>0)}}{d^{(i)}} = \sqrt{\frac{2\left(\frac{R}{d^{(i)}}\right) + 2n - 1}{1 + S_z} + \left(\frac{R_{n-1}^{(V>0)}}{d^{(i)}}\right)^2 - \left(\frac{R_{n-1}^{(V>0)}}{d^{(i)}}\right)} \quad n = 1, 2, \dots, N \quad (3)$$

$$j: \quad T_j^{(i)} = \lambda_j^{(i)} \cdot \frac{\partial w}{\partial \lambda_j} \Big|^{(i)} - p_h^{(i)} \quad j = x, y, z \quad (4)$$

$$r: \quad -p_{r,n}^{(V=0)} = \lambda_z^{(i)} \cdot \frac{\partial w}{\partial \lambda_z} \Big|^{(i)} - p_{h,n}^{(V=0)}$$

$$\varphi: \quad T_{\varphi,n}^{(V=0)} = \lambda_y^{(i)} \cdot \frac{\partial w}{\partial \lambda_y} \Big|^{(i)} - p_{h,n}^{(V=0)} \quad (5)$$

$$z: \quad T_{z,n}^{(V=0)} = \lambda_x^{(i)} \cdot \frac{\partial w}{\partial \lambda_x} \Big|^{(i)} - p_{h,n}^{(V=0)}$$

$$p = \varepsilon_0 \varepsilon_r \left( \frac{V}{d^{(i)}} \right)^2 \quad (6)$$

$$r: \quad -p_{r,n}^{(V>0)} = \lambda_z^{(i)} \cdot \frac{\partial w}{\partial \lambda_z} \Big|^{(i)} - p_{h,n}^{(V>0)}$$

$$\varphi: \quad T_{\varphi,n}^{(V>0)} = \lambda_y^{(i)} \cdot \frac{\partial w}{\partial \lambda_y} \Big|^{(i)} - p_{h,n}^{(V>0)} \quad (7)$$

$$z: \quad T_{z,n}^{(V>0)} = \lambda_x^{(i)} \cdot \frac{\partial w}{\partial \lambda_x} \Big|^{(i)} - p_{h,n}^{(V>0)}$$

$$F_{com} = (F_{spring}^{(V=0)} - F_{film,z}^{(V>0)}) - (F_{spring}^{(V=0)} - F_{film,z}^{(V=0)}) = \sum_{n=1}^N A_{z,n}^{(V=0)} \cdot \underbrace{(T_{z,n}^{(V=0)} - T_{z,n}^{(V>0)})}_p = A_{film,z}^{(V=0)} \cdot \varepsilon_0 \varepsilon_r \left( \frac{V}{d^{(i)}} \right)^2 \quad (8)$$

$$F_z^{(V>0)} = F_z^{(V=0)} - \sum_{n=1}^N p_n^{(V>0)} \cdot A_{z,n}^{(V>0)} = \dots = F_z^{(V=0)} - \varepsilon_0 \varepsilon_r V^2 \cdot \pi \sum_{n=1}^N \left[ 2 \left( \frac{R_n^{(V>0)}}{d_n^{(V>0)}} \right) - 1 \right] \quad (9)$$

## Figures

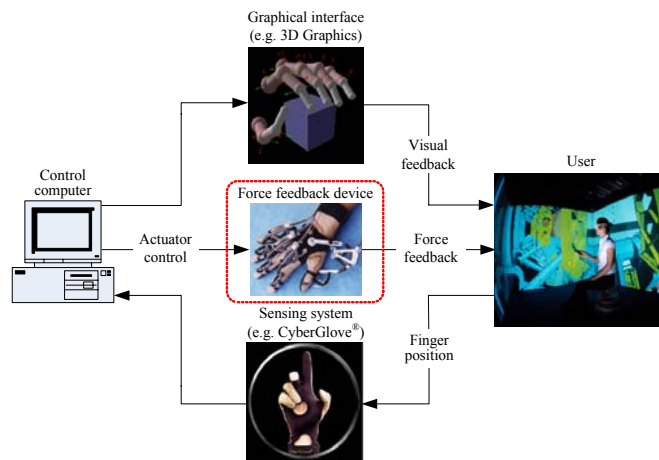


**Figure 22.1** Schematic of a force feedback system. Pictures of the CyberGlove and the CyberGrasp [3] are included to give a comprehensive overview.

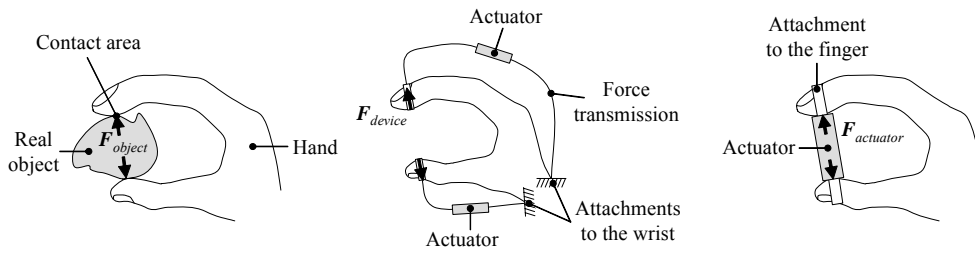


**Figure 22.2** Left: Reaction forces from a real object blocking the fingers' flexion during precision grasping. Center: Schematic of a conventional FFD. Right: Force feedback concept with minimal kinematics.

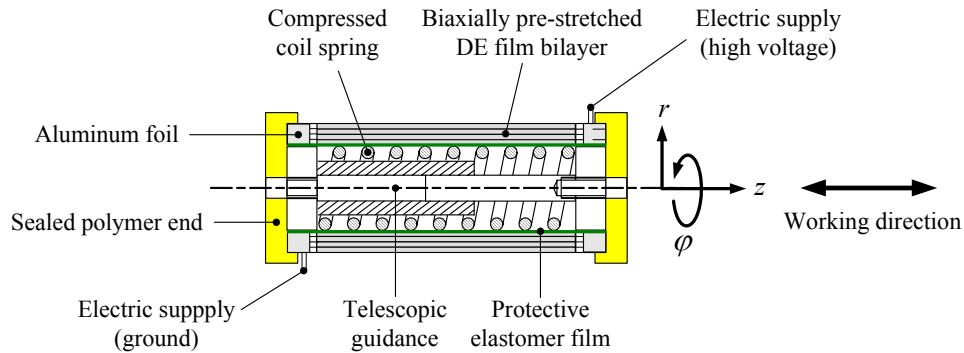


**Figure 22.3** Schematic of the design of rolled DE actuators.

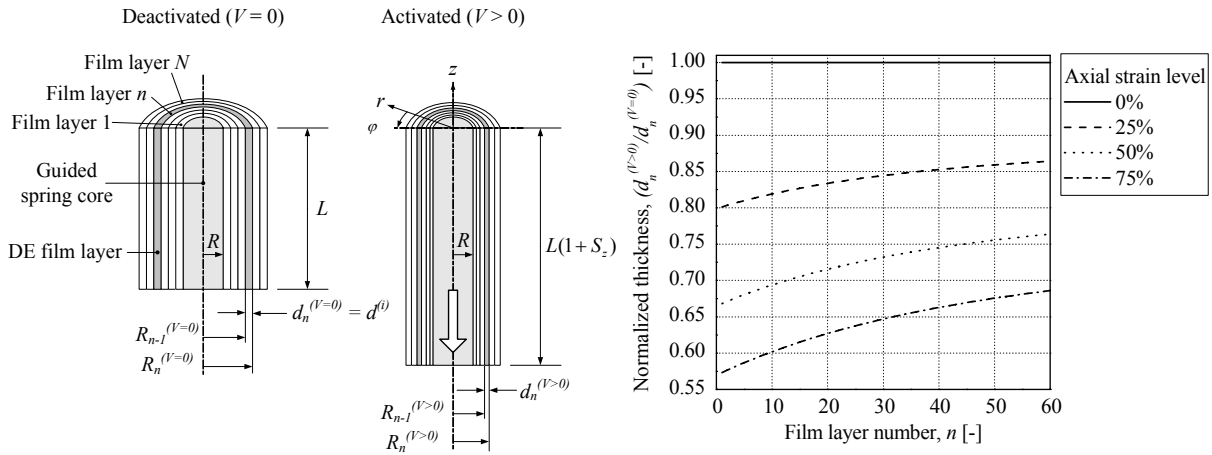


**Figure 22.4** Left and center: Idealized rolled DE actuator in the free-standing and axially elongated state. Right: Normalized thickness distribution of the film layers of the axially elongated actuator.

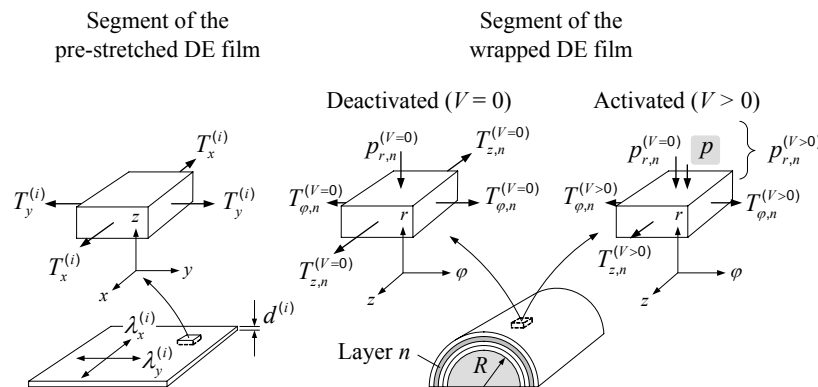


**Figure 22.5 Left:** Stretch state of a biaxially pre-stretched DE film. **Right:** Stretch state of a wrapped DE film layer in deactivated ( $V = 0$ ) and activated ( $V > 0$ ) condition.

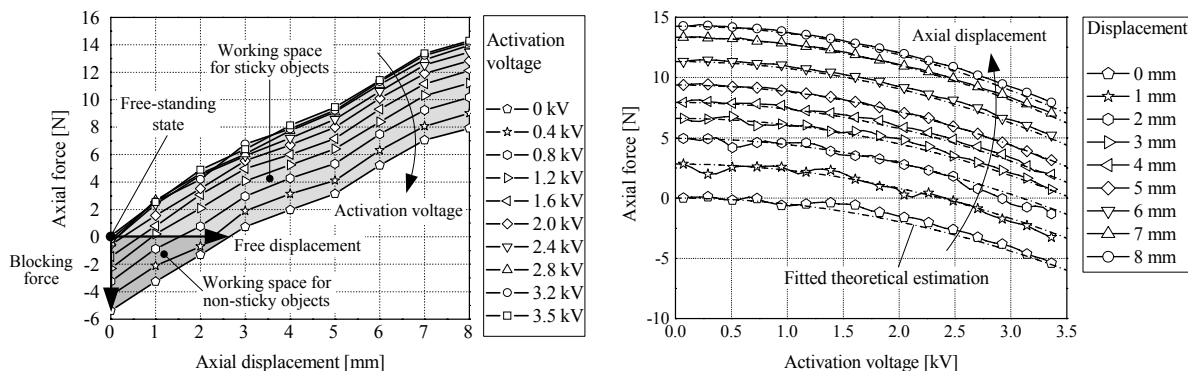


**Figure 22.6 Left:** Force-displacement behavior of the miniature rolled DE actuators at different activation voltage levels. **Right:** Experimental and fitted theoretical force-voltage behavior of the miniature rolled DE actuators.

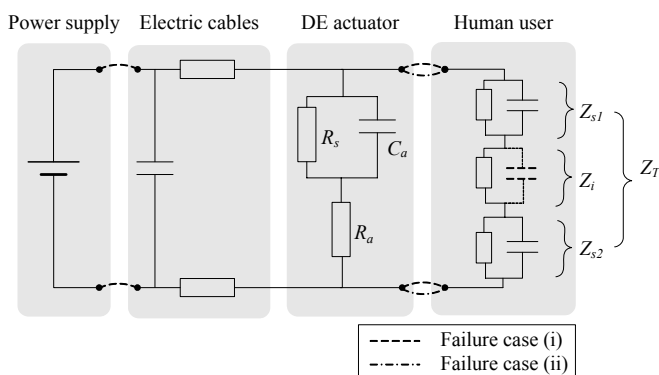


**Figure 22.7** Electrical model of the actuator-user system according to a FFD driven by the miniature rolled DE actuators.

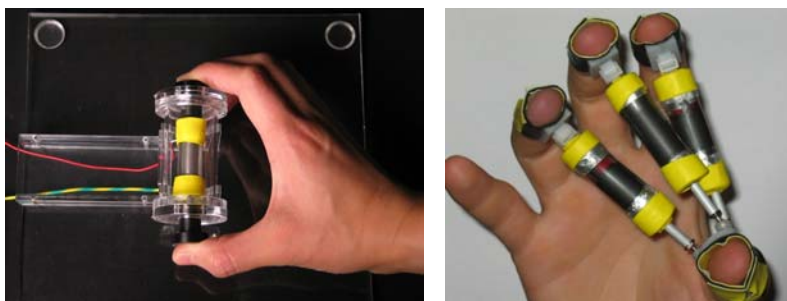


**Figure 22.8** Two demonstration devices for the generation of a force feedback with the miniature rolled DE actuators.